Chapter 2
Interconnect Modeling, CNT and GNR Structures, Properties, and Characteristics

Abstract This chapter reviews the Cu-based on-chip interconnect modeling. The unique atomic structure and properties of carbon nanotube (CNT) and graphene nanoribbon (GNR) are discussed. The characteristics and semiconducting/metallic properties of graphene-based on-chip interconnects are presented. Depending on the physical configuration, equivalent electrical models of MWCNT and MLGNR interconnect lines are also introduced. An extensive review on performance analysis of on-chip interconnects is presented.

Keywords Electrical equivalent model · Equivalent single conductor (ESC) · Lüttinger liquid theory · Multiconductor transmission line (MTL) · Tight-binding approximation

2.1 Interconnect Modeling Approaches

In the early days of VLSI design, the crosstalk-induced signal integrity effects were negligible because of relatively low integration density and slow operating speed. However, with the introduction of technology scaling of below 0.25 μm, there were many significant changes in the structure and electrical characteristics [1, 2]. The interconnect lines started to be a dominating factor for chip performance and robustness. The line parasitic elements have a major impact on the electrical behavior of the interconnect model. These models vary from simple to very complex depending upon the effects that are being studied and the required accuracy. There are three different types of approaches available in literature for modeling Cu-based on-chip interconnects.

2.1.1 Lumped Model with CMOS Driver

This approach focuses on the CMOS gate modeling while the interconnect line is approximately considered as a lumped circuit. Alpha-power law model [3] has been

© The Author(s) 2016

B.K. Kaushik et al., *Crosstalk in Modern On-Chip Interconnects*,
SpringerBriefs in Applied Sciences and Technology,
DOI 10.1007/978-981-10-0800-9_2

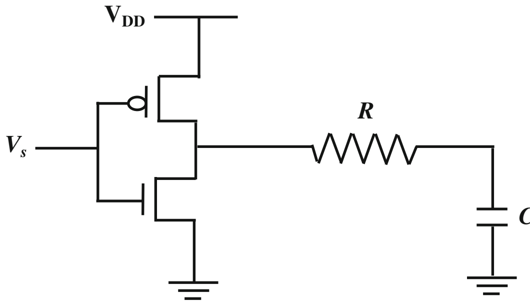

Fig. 2.1 A CMOS gate-driven *RC* load

widely used for representation of short-channel transistor that includes the velocity saturation effects. Based on the alpha-power law model, delay formulas were developed for CMOS gate-driven lumped capacitance modeled interconnect line [4, 5]. Bisdounis et al. [6] extended the model to include the influences of short-circuit current and gate-to-drain coupling capacitance. With the resistive component of interconnect becoming comparable to the gate output impedance, the line resistance *R* of interconnect line needs to be considered. Considering the line resistance, the modeling of CMOS gate-driven resistor-capacitor (*RC*) line was presented in [7–9]. The representation of CMOS gate-driven lumped *RC* load is shown in Fig. 2.1. Alder and Friedman [10] derived the delay equations for repeater insertion of a CMOS buffer design with *RC* interconnects. They developed a closed-form expression for the timing analysis of CMOS gate-driven *RC* load. They also derived an expression for the short-circuit power dissipation of the driver-interconnect-load system. However, all these approaches [3–10], lumped the total wire resistance of each segment into one single *R* and similarly combined the global capacitance into a single capacitor *C*. This lumped *RC* model is inaccurate for long interconnect wires, which are more adequately represented by a distributed *RC* model. Moreover, due to high operating frequencies and wider interconnect dimensions, interconnects exhibit inductance effects and should be included in the delay and crosstalk noise models. Hence, the analytical models that considered only *RC* were no longer accurate [3–10].

2.1.2 Distributed Model with Resistive Driver

In the distributed model with resistive driver, the driver-interconnect-load system is analyzed by simplifying the CMOS gate driver as a resistive driver [11]. Using the linear driver approximation, Elmore delay model was initially developed for *RC* lines [12] and then extended to *RLC* lines [13, 14]. The distributed *RLC* line with linear driver is shown in Fig. 2.2, where R_d and C_L represent driver resistance and load capacitance, respectively; *r*, *l* and *c* represent per-unit-length line resistance,

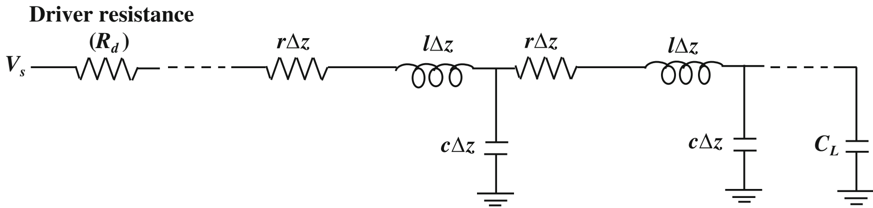

Fig. 2.2 A distributed *RLC* interconnect line driven by a resistive driver

inductance, and capacitance, respectively. Considering the nonlinearity of the driver, Bai et al. [15] improved the linear driver model by calculating the effective resistance. Davis and Meindl proposed closed-form delay expressions for the analysis of distributed *RLC* lines by considering the single transmission line effects in [16] and a crosstalk noise model of coupled transmission lines in [17].

Based on even–odd mode technique, the crosstalk noise model was developed by Agarwal et al. [18] for coupled-two lossless lines and then modified for low-loss lines to analyze crosstalk-induced noise peak voltage. They investigated that at high operating frequencies, inductive coupling effects are significant and should be included for accurate crosstalk noise analysis. Using the coupled transmission line theory, the authors developed a crosstalk noise model that is useful to guide noise-aware physical design optimizations. A closed-form analytical transient response model was derived for resistance/capacitance loads by solving semifinite transmission line equations [19]. However, all these models [11–19] consider the nonlinear CMOS driver as a linear driver that limits the accuracy of the models.

2.1.3 Distributed Model with CMOS Driver

The distributed model with CMOS driver approach co-simulates the nonlinear CMOS gate and the distributed interconnect. The CMOS gate-driven distributed *RLC* interconnect line is shown in Fig. 2.3. Based on the even–odd modes, Kaushik et al. proposed a simple analytical model for functional crosstalk analysis in [20] and dynamic crosstalk analysis in [21] of CMOS gate-driven two coupled

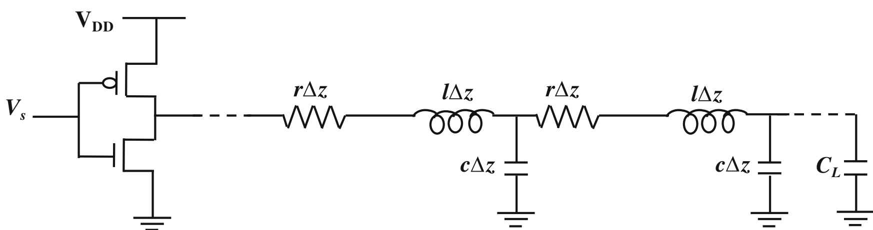

Fig. 2.3 A CMOS gate-driven distributed *RLC* interconnect line

interconnect lines. The model was developed based on the alpha-power law model of MOS transistors and transmission line theory of interconnects. There the authors have observed that the nonlinear effects of the CMOS inverter should be incorporated in a valid crosstalk noise modeling. Moreover, it was noticed that the use of resistive driver model presented a pessimistic view on the performance analysis of on-chip interconnects. However, these models [20, 21] were based on the even–odd modes and hence limited to two coupled interconnect lines. Later on, Li et al. [22] proposed an FDTD method for the transient analysis of CMOS gate-driven lossy transmission lines including frequency-dependent losses and observed the effect of functional crosstalk. However, the model ignored the finite drain conductance parameter in the modeling of CMOS driver and hence not useful for nanoscaled devices.

2.2 Carbon Nanotubes

Until mid-1980s, diamond and graphite were the only two known forms of carbon allotropes. In 1985, Kroto et al. [23] were able to synthesize new allotrope of carbon C_{60}. They used a high pulse of laser light to vaporize a sample of graphite. The vaporized graphite was sent to a mass spectrometer with the help of helium gas. The mass spectrometer detected the presence of C_{60}, a molecule consisting of 60 carbon atoms. The C_{60} had the shape of a soccer ball with 12 pentagon faces and 20 hexagonal faces. The easy synthesis of C_{60} led the group to propose the existence of another allotrope of carbon named as "buckyball" due to its soccer ball-shaped structure. The shape of the new allotrope of carbon did not end at the soccer-shaped structures and long cylindrical tube-like structures were also reported, which are known as carbon nanotubes (CNTs).

CNTs have fascinated the research world due to their extraordinary physical, electrical, and chemical properties. Many of the properties defy the conventional trends and scientists are still discovering the unique properties and constantly making efforts to understand and explain the phenomenon for such distinctive behavior. One of the remarkable physical properties of CNT is its ability to scale down its thickness to a single atomic layer. Another interesting physical property observed in CNTs is when two slightly different-structured CNTs are joined together; the resultant junction formed can be used as an electronic device. The properties of the device formed are dependent on the type of CNTs used for their formation.

2.2.1 Basic Structure of CNTs

A single-walled CNT can be assumed as a structure formed when a single graphene sheet is rolled into a cylindrical shape (Fig. 2.4). Depending on the shape of the

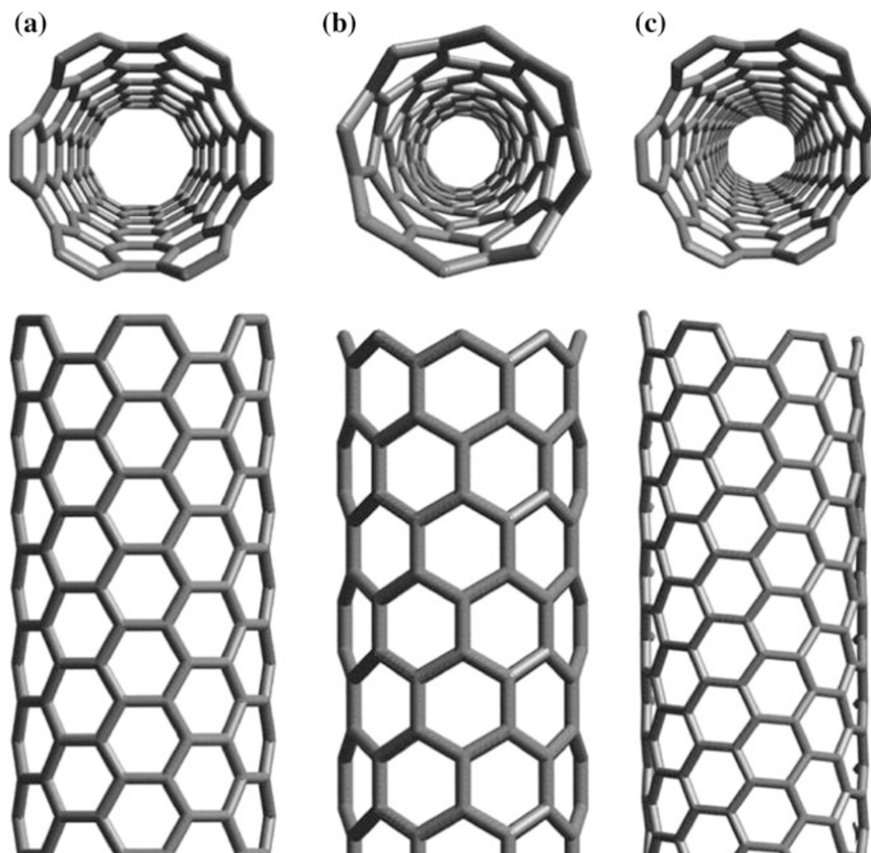

Fig. 2.4 Sketches of three different SWCNT structures: **a** armchair nanotube, **b** zigzag nanotube, and **c** chiral nanotube

circumference, CNTs can be classified as armchair (ac), zigzag (zz), or chiral CNTs as shown in Fig. 2.4a–c, respectively [24]. The terms zigzag and armchair are inspired from the pattern in which the carbon atoms are arranged at the edge of the nanotube cross section. Graphene consists of sp^2-hybridized atoms of carbon that are arranged in a hexagonal pattern. The hexagonal carbon rings should join coherently when placed in contact with adjacent carbon atoms. Accordingly, in an SWCNT tube, all the carbon atoms (except at the edges) form hexagonal rings and are therefore equally spaced from one another. Xu et al. [25] reported the fabrication of vertically grown CNT bundles with an average diameter of 50 μm and a pitch of 110 μm.

In spite of the hexagonal aromatic rings, SWCNT is considered to be more reactive than planar graphene. It is due to the fact that the hybridization in SWCNTs is not purely sp^2 and some degree of sp^3 hybridization is also present. It has been observed that with the decrease in SWCNT diameter, the degree of sp^3

hybridization increases [26]. This phenomenon causes variable overlapping of energy bands that results in SWCNTs obtaining versatile and unique electrical properties. It was studied that beyond the diameter of ≈2.5 nm, the SWCNT tube collapses into a two-layer ribbon [26]. Moreover, a CNT with smaller diameter results in higher stress on the structure, although SWCNTs of ≈0.4 nm diameter have been produced [27]. It is therefore natural to consider that a diameter of ≈1 nm is the most suitable value with regard to energy consideration of SWCNTs. Encouragingly, there are no such restrictions on the length of the SWCNTs. The length is dependent on the processes and methods used for synthesis of the SWCNTs. SWCNTs of length ranging from micrometers to millimeters can be commonly observed. Considering the diameter and length of an SWCNT, it is easy to intuitively conclude that SWCNT structures have exceptionally high aspect ratios.

A graphene sheet can be rolled in a number of different ways (see Fig. 2.4). The mathematical expression that can be used to represent the various ways of rolling graphene into the tubes is shown below [28]:

$$PX = \boldsymbol{C}_h = p\boldsymbol{b}_1 + q\boldsymbol{b}_2 \tag{2.1}$$

where $\boldsymbol{C}_h$ is chirality vector, p and q are integers. The unit vectors $\boldsymbol{b}_1$ and $\boldsymbol{b}_2$ are defined as

$$\boldsymbol{b}_1 = \frac{b\sqrt{3}}{2}\boldsymbol{x} + \frac{b}{2}\boldsymbol{y} \quad \text{and} \quad \boldsymbol{b}_2 = \frac{b\sqrt{3}}{2}\boldsymbol{x} - \frac{b}{2}\boldsymbol{y} \tag{2.2}$$

where b = 2.46 Å and $\cos\theta = \frac{2p+q}{2\sqrt{p^2+q^2+pq}}$.

The vector PX is normal to the CNT tube axis and θ is chirality angle. The diameter d of a nanotube is dependent on $\boldsymbol{C}_h$ by the following relation:

$$d = \frac{|C_h|}{\pi} = \frac{b_{\mathrm{C-C}}\sqrt{3(p^2+q^2+pq)}}{\pi} \tag{2.3}$$

where $1.41\ \text{Å(graphene)} \leq b_{\mathrm{C-C}} \leq 1.44\ \text{Å}(\mathrm{C}_{60})$.

The C–C bond length in the hexagonal ring structure of SWCNT slightly increases from the C–C bond length in graphene due to the curved structure of SWCNT. The degree of curvature in an SWCNT cannot exceed the degree of curvature in C_{60} molecule, resulting in the upper limit of C–C bond length in SWCNTs. Similarly, the degree of curvature in an SWCNT cannot be less than the curvature in a flat graphene structure, resulting in lower limit of C–C bond length in SWCNTs. Moreover, it can be observed that $\boldsymbol{C}_h$, θ, and d can be expressed in terms of p and q. Since SWCNTs can be identified by $\boldsymbol{C}_h$, θ, and d values, it is sufficient to define SWCNTs through p, q values by denoting them as (p, q). The p and q values for a particular SWCNT can be easily obtained by counting the number of hexagonal rings separating the margins of $\boldsymbol{C}_h$ vector following $\boldsymbol{b}_1$ first and then $\boldsymbol{b}_2$

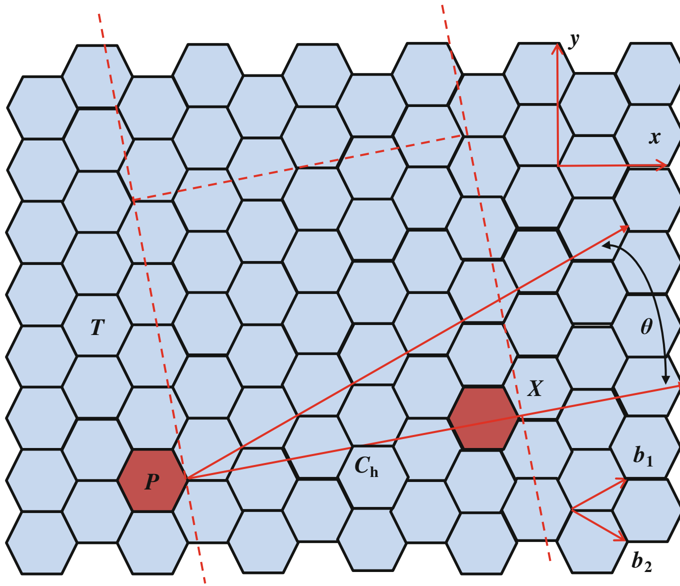

Fig. 2.5 Sketch representing the procedure to obtain a CNT, starting from a graphene sheet

[29]. Based on the (p, q) representation, zz SWCNTs can be denoted as (p, 0) and having $\theta = 0°$; ac SWCNTs can be denoted as (p, p) and having $\theta = 30°$; chiral SWCNTs can be denoted as (p, q) and having $0 < \theta < 30°$.

From Fig. 2.5, it can be observed that having $\boldsymbol{C}_h$ direction perpendicular to any carbon bond directions results in zz SWCNT ($\theta = 0°$), while having $\boldsymbol{C}_h$ direction parallel to any carbon bond directions will result in ac SWCNT ($\theta = 30°$). In chiral SWCNTs, $0 < \theta < 30°$ due to hexagonal rings in graphene sheet.

An MWCNT is a bit more intricate in structure compared to an SWCNT. Unlike a single graphene shell in an SWCNT, there are multiple graphene shells in an

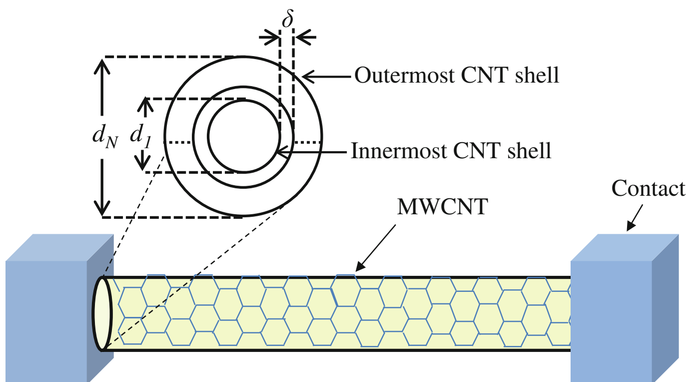

Fig. 2.6 The structure of MWCNT placed between the two contacts

MWCNT. The MWCNTs have two or more numbers of CNT shells that are concentrically rolled up. The structure of MWCNT between the two contacts is shown in Fig. 2.6, wherein the inset figure shows its cross-sectional view. The intershells are separated by the van der Waals gap, $\delta \sim 0.34$ nm. The diameter of outermost CNT shell can be varied from a few nanometers to several tens of nanometers. The diameters of outermost and innermost shells are denoted by d_N and d_1, respectively. The ratio of d_1/d_N varies in different MWCNTs, the values between 0.3 and 0.8 have been observed in [30–32]. The density of 10^6/cm^2 has been obtained in [30] with a d_1/d_N of 0.5. The current carrying capabilities of MWCNTs are similar to the SWCNT bundles, however, the MWCNTs are easier to fabricate [33]. Close et al. [34] reported the fabrication of MWCNTs with 80 shells based on a versatile method that is ideally suited for fabricating MWCNT interconnects with extensive electrical properties.

2.2.2 Semiconducting and Metallic CNTs

CNTs can act as semiconducting or metallic based on the pattern of CNT circumference. The armchair CNTs always act as metallic, whereas the zigzag CNTs act as either metallic or semiconducting depending on the chiral indices. This section presents the behavior of zz CNTs and their dual nature.

Since CNT is a rolled-up sheet of graphene, an appropriate boundary condition is required to explore the band structure. If CNT can be considered as an infinitely long cylinder, there are two wave vectors associated with it: (1) the wave vector parallel to CNT axis, $k_{\parallel}$, that is continuous in nature due to the infinitely long length of CNTs and (2) the perpendicular wave vector, $k_{\perp}$, that is along the circumference of the CNT. These two wave vectors must satisfy a periodic boundary condition [28]

$$k_{\perp}.C_h = \pi d k_{\perp} = 2\pi m \tag{2.4a}$$

where m is an integer. The quantized values of allowed $k_{\perp}$ for CNTs are obtained from the boundary condition. The cross-sectional cutting of the energy dispersion with the allowed $k_{\perp}$ states results in the one-dimensional band structure of graphene as shown in Fig. 2.7a. This is called zone folding scheme of obtaining the band structure of CNTs. Each cross-sectional cutting gives rise to one-dimensional subband. The spacing between allowed $k_{\perp}$ states and their angles with respect to the surface Brillouin zone determine the one-dimensional band structures of CNTs. The band structure near the Fermi level is determined by allowed $k_{\perp}$ states that are close to the K points. When the allowed $k_{\perp}$ states pass directly through the K points as shown in Fig. 2.7c, the energy dispersion has two linear bands crossing at the Fermi level without a bandgap. However, if the allowed $k_{\perp}$ states miss the K points as shown in Fig. 2.7b, there would be two parabolic one-dimensional bands with an energy bandgap. Therefore, two different kinds of CNTs can be expected depending on the wrapping indices, first, the semiconducting CNTs with bandgap as in Fig. 2.7b and second, the metallic CNTs without bandgap as in Fig. 2.7c [28].

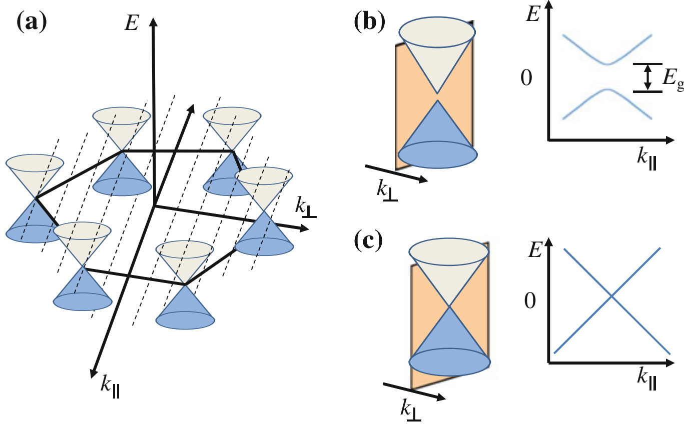

Fig. 2.7 Band structures of CNT shell **a** first Brillouin zone of graphene with conic energy dispersions at six K points. The allowed $k_\perp$ states in CNT are presented by dashed lines. The band structure of the CNT is obtained by the cross sections as indicated. Close view of the energy dispersion near one of the K points are schematically shown along with the cross sections by allowed $k_\perp$ states and resulting one-dimensional energy dispersions for **b** a semiconducting CNT and **c** a metallic CNT

Using the approach of one-dimensional subbands discussed in previous sub-section, the one-dimensional subband closest to the K points for zigzag CNTs is investigated here. Based on the chiral indices, the zigzag CNTs can show metallic/semiconducting property. Since the circumference is $\bar{p} \cdot b(C_\mathrm{h} = \bar{p} \cdot b_1)$, the boundary condition in Eq. (2.4a) becomes

$$k_x \bar{p} b = 2\pi m \tag{2.4b}$$

There is an allowed k_x that coincides with K point at (0, 4π/3b). This condition arises when $\bar{p}$ has a value in multiples of 3 ($\bar{p} = 3\bar{q}$, where $\bar{q}$ is an integer). Therefore, by substitution in Eq. (2.4b) [28]

$$k_x = \frac{2\pi m}{\bar{p} b} = \frac{3Km}{2\bar{p}} = \frac{Km}{2\bar{q}} \tag{2.5}$$

There is always an integer $(m = 2\bar{q})$ that makes k_x pass through K points and these types of CNTs (with $\bar{p} = 3\bar{q}$) are always metallic without bandgap as shown in Fig. 2.7c. There are two cases when p is not a multiple of 3. If $\bar{p} = 3\bar{q} + 1$, the k_x is closest to the K point at $m = 2\bar{q} + 1$ (as in Fig. 2.7b).

$$k_x = \frac{2\pi m}{\bar{p} b} = \frac{3Km}{2\bar{p}} = \frac{3K(2\bar{q} - 1)}{2(3\bar{q} + 1)} = K + \frac{K}{2} \frac{1}{3q + 1} \tag{2.6}$$

Similarly, for $\bar{p} = 3\bar{q} - 1$, the allowed k_x closest to K is when $m = 2\bar{q} - 1$, hence

$$k_x = \frac{2\pi m}{\bar{p}b} = \frac{3Km}{2\bar{p}} = \frac{3K(2\bar{q} - 1)}{2(3\bar{q} - 1)} = K - \frac{K}{2}\frac{1}{3\bar{q} - 1} \tag{2.7}$$

In these two cases, allowed k_x misses the K point by

$$\Delta k_x = \frac{K}{2}\frac{1}{3\bar{q} \pm 1} = \frac{2}{3}\frac{\pi}{\bar{p}b} = \frac{2}{3}\frac{\pi}{\pi d} = \frac{2}{3d} \tag{2.8}$$

From Eq. (2.8), it is inferred that the smallest misalignment between an allowed k_x and a K point is inversely proportional to the diameter. Thus, from the slope of a cone near K points in Eq. (2.4a), the bandgap E_g can be expressed as

$$E_g = 2 \times \left(\frac{\partial E}{\partial k}\right) \times \frac{2}{3d} = 2\hbar v_F \left(\frac{2}{3d}\right) \approx 0.7\text{eV}/d\,(\text{nm}) \tag{2.9}$$

Therefore, semiconducting CNTs (d = 0.8–3 nm) exhibit bandgap ranging from 0.9 to 0.2 eV. Depending on the value of $\bar{p}$, where $\bar{p}$ is the remainder when p and q is divided by 3, SWCNTs [represented by (p, q)] can be of three types:

$\bar{p} = 0$; metallic with linear subbands crossing at the K points.
$\bar{p} = 1, 2$; semiconducting with a bandgap, E_g ~ 0.7 eV/d (nm).

Similar treatment can also be applied for armchair CNTs $(\bar{p}, \bar{p})$, arriving at the conclusion that they are always metallic.

2.2.3 *Properties and Characteristics of CNTs*

The atomic arrangements of carbon atoms are responsible for the unique electrical, thermal, and mechanical properties of CNTs [35, 36]. The sp^2 bonding delivers the high conductivity and mechanical strengths to the CNTs. The unique properties of CNTs are discussed below.

2.2.3.1 Strength and Elasticity

Due to the sp^2-hybridization, each carbon atom in a single sheet of graphite is connected via strong sigma bonds to three neighboring atoms. Thus, CNTs exhibit the strongest basal plane elastic modulus and hence are expected to be the ultimate high-strength fiber. The elastic modulus of CNT is much higher than steel that makes the CNT as a strongest material. Although forcing on the tip of nanotube will cause it

to bend, the nanotube returns to its original state as soon as the force is removed. This property makes CNTs extremely useful as probe tips for high-resolution scanning probe microscopy. Although, the current Young's modulus of SWCNT is about 1 TPa, but a much higher value of 1.8 TPa has also been reported [37]. For different experimental measurement techniques, the values of Young's modulus vary in the range of 1.22–1.26 TPa depending on the size and chirality of the SWCNTs [36]. It has been observed that the elastic modulus of CNTs is not strongly dependent on the diameter. Primarily, the moduli of CNTs correlate to the amount of disorder in the nanotube walls [38].

2.2.3.2 Thermal Conductivity and Expansion

CNTs can exhibit superconductivity below 20 K (−253 °C) due to the strong in-plane sigma bonds in between carbon atoms. The sigma bond provides exceptional strength and stiffness against axial strains. Moreover, the larger interplane and zero in-plane thermal expansion of SWCNTs results in high flexibility against nonaxial strains.

Due to their high thermal conductivity and large in-plane expansion, CNTs exhibit exciting prospects in nanoscale molecular electronics, sensing and actuating devices, reinforcing additive fibers in functional composite materials, etc. Recent experimental measurements suggest that the CNT-embedded matrices are stronger in comparison to bare polymer matrices [39]. Therefore, it is expected that the nanotube may also significantly improve the thermomechanical and the thermal properties of the composite materials.

2.2.3.3 Field Emission

Under the application of strong electric field, tunneling of electrons from the metal tip to vacuum results in the phenomenon of field emission. Field emission results from the high aspect ratio and small diameter of CNTs. The field emitters are suitable for the application in flat panel displays. For multiwalled CNTs, the field emission properties occur due to the emission of electrons and light. Without applied potential, the luminescence and light emission occur through the electron field emission and visible part of the spectrum, respectively.

2.2.3.4 Aspect Ratio

One of the exciting properties of CNTs is the high aspect ratio, which infers that a lower CNT load is required compared to other conductive additives to achieve

similar electrical conductivity. The high aspect ratio provides unique electrical conductivity in CNTs in comparison to the conventional additive materials such as chopped carbon fiber, carbon black, or stainless steel fiber.

2.2.3.5 Absorbent

Carbon nanotubes and CNT composites have been emerging as perspective absorbing materials due to their light weight, larger flexibility, high mechanical strength, and large surface area. Therefore, CNTs emerge out as ideal candidates for use in gas, air, and water filtration. The absorption frequency range of SWCNT–polyurethane composites broaden from 6.4–8.2 (1.8 GHz) to 7.5–10.1 (2.6 GHz) and to 12.0–15.1 GHz (3.1 GHz) [40]. A lot of research has already been carried out for replacing the activated charcoal with CNTs for certain ultra-high purity applications [41].

2.2.3.6 Conductivity

CNTs are assumed to be the most electrically conductive materials. However, it is quite difficult to control the chirality of the SWCNT shells and therefore statistically only one-third of the CNTs in a bundle is assumed to be conducting and the rest of them are semiconducting. However, because of large diameters, the CNT shells of MWCNTs would be conductive even if they are of semiconductor characteristics. The energy gap between the conduction band edge and the Fermi level of a CNT shell is defined as [30]

$$\boldsymbol{E}_g = \frac{v_0 p_{\mathrm{C-C}}}{d} \tag{2.10}$$

where d is the CNT diameter, v_0 is the nearest-neighboring tight-binding parameter, and $p_{\mathrm{C-C}}$ is the nearest neighbor C–C bond length, which is $\sim$0.142 nm. From Eq. (2.10), it can be observed that the bandgap is inversely proportional to the diameter. Therefore, the semiconducting CNT shells with larger diameter are conductive. The detailed conductivity comparison between MWCNTs and SWCNTs will be discussed in the following sections.

2.2.4 *Conductivity Comparison*

The performance of interconnect primarily depends on the conductivity of the interconnect filler material. The conductivity comparison among Cu, SWCNT, and MWCNT is analyzed in this section.

2.2.4.1 SWCNT Conductivity

The conductivity of SWCNT [42, 43] can be expressed as

$$\sigma_{\mathrm{SWCNT}} = \frac{4G_0 l_0 d F_m}{\sqrt{3}(d+\delta)^2} \frac{l}{(l + l_0 d)} \tag{2.11}$$

where l, d, F_m are the interconnect length, shell diameter, fraction of metallic CNTs in the bundle, respectively, l_0 is 10^3, δ is 0.34 nm, G_0 is the quantum conductance equal to $2e^2/h$, e is the charge of an electron, and h is the Planck's constant.

For $l > l_0 d$, Eq. (2.11) can be expressed as

$$\sigma_{\mathrm{SWCNT}} \approx \frac{4G_0 l_0 d F_m}{\sqrt{3}(d+\delta)^2} \tag{2.12}$$

From Eq. (2.12), it can be observed that for longer interconnects, the conductivity of SWCNT is independent of length.

2.2.4.2 MWCNT Conductivity

The conductivity of MWCNT [44] can be expressed as

$$\sigma_{\mathrm{MWCNT}} = \frac{G_0 l}{2\delta}\left[\left(1 - \frac{d_{\min}^2}{d_{\max}^2}\right)\frac{a}{2} + \left(b - \frac{l}{l_0}a\right) \times \left(\left(\frac{1}{d_{\max}} - \frac{d_{\min}}{d_{\max}^2}\right) - \frac{l}{d_{\max}^2 l_0}\ln\frac{d_{\max} + \frac{l}{l_0}}{d_{\min} + \frac{l}{l_0}}\right)\right] \tag{2.13}$$

where $d_{\max}$ and $d_{\min}$ are the outermost and the innermost shell diameters of an MWCNT, respectively; a and b are constants and the values are 0.0612 nm^{-1} and 0.425, respectively [45]. From Eq. (2.13), it can be observed that for $l > (l_0 b/a)$, the conductivity increases with an increase in $d_{\max}$.

The conductivity comparison plot among Cu, SWCNT bundles, and MWCNT is shown in Fig. 2.8. It can be observed that for shorter interconnect length, the conductivity of SWCNT bundle is higher than MWCNT, whereas for longer lengths, MWCNTs can potentially have conductivities several times larger than that of copper or even SWCNT, which is essential for interconnect applications. It is worth noting that the best case scenario is considered for SWCNTs, wherein they were densely packed so that highest conductivity is obtained. However, in contrast to this, an average case scenario was considered for MWCNTs wherein the innermost diameter is half of the outermost shell diameter. The innermost diameters were considered as 5, 15, 35, 50 nm for respective outer diameters of 10, 30, 70, 100 nm. However, the best case scenario for MWCNTs would have been when the innermost diameter had been 1 nm. But still, for longer interconnects, the performance of the MWCNTs was better than the SWCNTs.

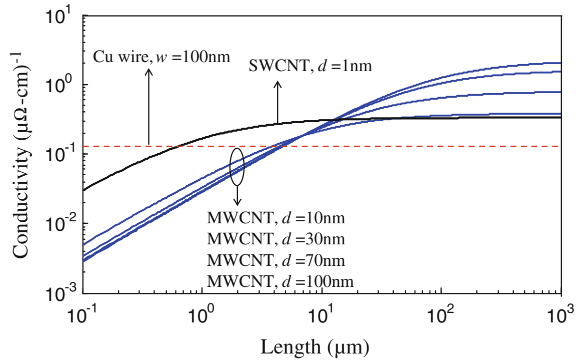

Fig. 2.8 The conductivity comparison among Cu, SWCNT, and MWCNT

2.2.5 *MWCNT Interconnect Modeling*

MWCNTs have recently acquired importance for VLSI on-chip interconnect material due to their high current carrying capabilities. For the first time, Burke [46] proposed an electrical equivalent model for the analysis of CNT interconnects based on the Lüttinger liquid theory. The model considered the quantum effects of a nanowire by including the quantum resistance, kinetic inductance, and quantum capacitance. The electrical equivalent model was further explained by Avouris et al. [47] through extensive study of electronic structure and transport properties of CNTs. Depending on the analysis, a bottom-up approach was demonstrated by Li et al. [48] to integrate MWCNTs into multilevel interconnects in silicon-integrated circuits. Ngo et al. [49] reported the mechanism of electron transport across metal–CNT interface. The authors analyzed this mechanism for two different MWCNT architectures, horizontal or side-contacted MWCNTs and vertical or end-contacted MWCNTs. Later, Miano and Villone [50] extended the fluid theory model for frequency domain to describe the electromagnetic response of three-dimensional (3D) structures formed by metallic CNTs and conductors within the framework of classical electrodynamics.

Xu and Srivastava [51] presented a semiclassical one-dimensional (1D) electron fluid model that took into account the electron–electron repulsive force. Based on the one-dimensional electron fluid theory, the authors presented a transmission line model of metallic CNT interconnects using classical electrodynamics. However, the authors neglected the inter-CNT tunneling phenomenon. Later, Li et al. [43] presented a multiconductor transmission line (MTL) model for the MWCNT. The authors considered the tunneling effect between the adjacent shells in MWCNT and neighboring CNTs in a bundle. However, using the MTL model, the analysis of MWCNT with N number of tubes leads to the solution of differential equations with the system dimensional of $2N$, which can be computationally expensive. For this reason, the equivalent single conductor (ESC) model was proposed in [52].

The ESC model is based on the assumption that voltages at an arbitrary cross section along MWCNT are the same, such that all nanotubes are connected in parallel at both ends. The accuracy of the ESC model in comparison to MTL model has been reported by several researchers [52, 53]. It was observed that the transient responses to a pulse input of MTL model and ESC model are in good agreement. The MTL and ESC models are briefly described in the next section.

2.2.5.1 MTL and ESC Models of MWCNT Interconnect

The electrical equivalent models of MWCNT interconnect are discussed in this section. The schematic cross-sectional view of MWCNT interconnect is shown in Fig. 2.9. The MWCNT bundle interconnect line is positioned over a ground plane at a distance H and placed in a dielectric medium with dielectric constant ε. The MWCNT interconnect consists of N number of tubes with intershell distance δ, inner shell diameter d_1, and outer shell diameter d_N. The total number of CNTs in an MWCNT can be expressed as

$$N = 1 + \text{int}\left[\frac{(d_N - d_1)}{2\delta}\right] \tag{2.14}$$

where int[•] represents an integer value. The number of conducting channels in a CNT can be derived by adding all the subbands contributing to the current conduction. Using Fermi function, it can be expressed as

$$N_{\text{ch},i} = \sum_{\text{subbands}} \frac{1}{\exp(|E_i - E_F|/k_B T) + 1} \tag{2.15}$$

where T is the temperature, k_B is the Boltzmann constant, and E_i is the lowest (or highest) energy for the subbands above (or below) the Fermi level E_F.

The multiconductor transmission line (MTL) model of MWCNT interconnect is described in Fig. 2.10, where $R_{MC,i}$ and $R_{Q,i}$ represent the imperfect metal contact

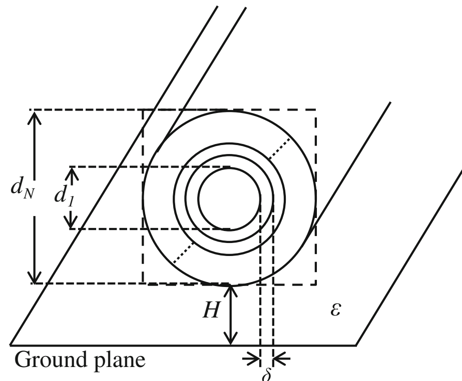

Fig. 2.9 Geometry of an MWCNT with N shells above a ground plane

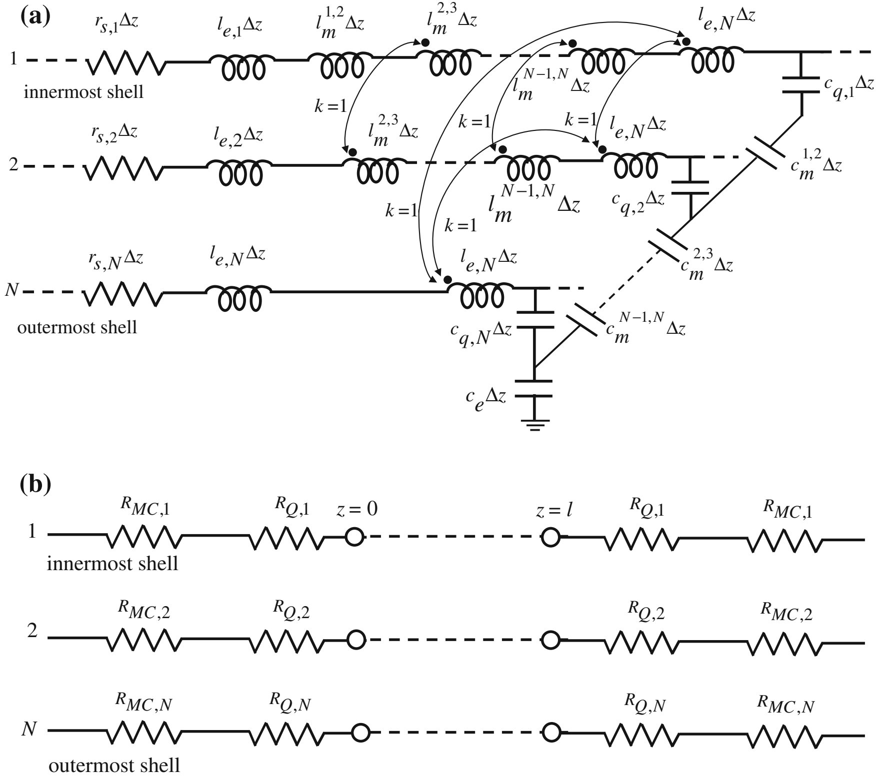

Fig. 2.10 Multiconductor transmission line model of MWCNT (**a**) section of infinitesimal length Δz, where $k = 1$ represents perfect magnetic coupling (**b**) nanotube of length l including terminal resistance

resistance and quantum resistance of ith shell, respectively; $r_{s,i}$, $l_{k,i}$, and $c_{q,i}$ represent the p.u.l. scattering resistance, kinetic inductance, and quantum capacitance, respectively. The parasitics $R_{Q,i}$, $r_{s,i}$, $l_{k,i}$, and $c_{q,i}$ can be expressed as

$$R_{Q,i} = \frac{h}{4e^2 N_{\mathrm{ch,i}}} \tag{2.16a}$$

$$r_{s,i} = \frac{h}{2e^2 \lambda_{\mathrm{mfp,i}} N_{\mathrm{ch,i}}} \tag{2.16b}$$

$$l_{k,i} = \frac{h}{4e^2 v_F N_{\mathrm{ch,i}}} \tag{2.16c}$$

$$c_{q,i} = \frac{4e^2 N_{\mathrm{ch,i}}}{h v_F} \tag{2.16d}$$

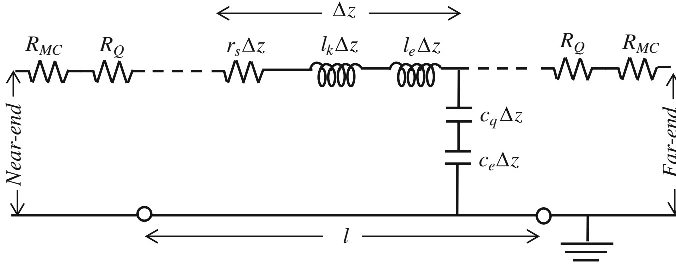

Fig. 2.11 Equivalent single conductor model of MWCNT

where h, e λ_{mfp}, and v_F represent the Planck's constant, electron charge, mean free path, and Fermi velocity, respectively.

In Fig. 2.10, $l_{e,i}$ is p.u.l. magnetic inductance of the ith shell and c_e is p.u.l. electrostatic capacitance, $c_m^{i,i+1}$ and $l_m^{i,i+1}$ are the p.u.l. coupling capacitance and mutual inductance between the shells, respectively. These parasitics can be expressed as

$$l_{e,i} = \frac{\mu_0 \mu_r}{2\pi} \cosh^{-1}\left[\left(\frac{d_i + 2H}{d_i}\right)\right] \tag{2.16e}$$

$$c_e = \frac{2\pi\varepsilon_0\varepsilon_r}{\cosh^{-1}\left[\left(\frac{d_N + 2H}{d_N}\right)\right]} \tag{2.16f}$$

$$c_m^{i,i+1} = \frac{2\pi\varepsilon_0}{\ln(d_{i+1}/d_i)}, \quad i = 1, 2, \ldots, N-1 \tag{2.16g}$$

$$l_m^{i,i+1} = \frac{\mu}{2\pi} \ln(d_{i+1}/d_i), \quad i = 1, 2, \ldots, N-1 \tag{2.16h}$$

To reduce the complexity of the MTL model, a simplified ESC model was proposed in [52]. The ESC model is shown in Fig. 2.11. This model was developed based on the assumption that voltages at an arbitrary cross section along MWCNT are the same. Thus, all the scattering resistances $r_{s,i}$ are in parallel and can be replaced by an equivalent resistance ($r_{s,\text{ESC}}$). The $r_{s,\text{ESC}}$ can be expressed as

$$r_{s,\text{ESC}} = \frac{h/e^2}{\sum_{i=1}^{N} 2N_{\text{ch},i}\lambda_{\text{mfp},i}} \tag{2.17a}$$

Referring to Fig. 2.12, the distributed MWCNT capacitance $c_{q,\text{ESC}}$ is expressed in terms of quantum capacitance and coupling capacitance between shell to shell.

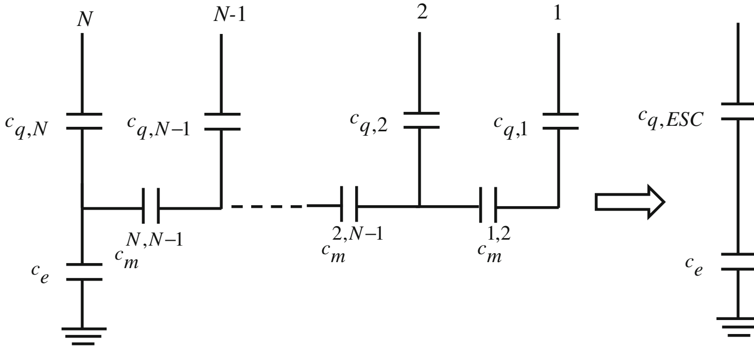

Fig. 2.12 Per unit length capacitance network of the MWCNT

$$c_{\text{equ},1} = c_{q,1} \tag{2.17b}$$

$$c_{\text{equ,i}} = \left(\frac{1}{c_{\text{equ,i}-1}} + \frac{1}{c_m^{i-1,\text{i}}} \right)^{-1} + c_{q,\text{i}}, \quad i = 2, 3, \ldots, N \tag{2.17c}$$

$$c_{q,\text{ESC}} = c_{\text{equ,N}} \tag{2.17d}$$

The inductance equations can be written in a similar form. The ESC model of MWCNT interconnect is thoroughly discussed in Sect. 4.2.

2.2.6 MWCNT Performance Analysis

The performance analysis of MWCNT interconnects was analyzed using both the MTL and ESC models in [54]. The voltage response of two coupled MWCNT interconnects of 14 and 22 nm technologies was computed to a pulse input. It was observed that both models are in good agreement. The same agreement was achieved in the estimation of 50 % time delay as well. The validity of the ESC model was also verified experimentally in [52]. Based on the ESC model, Lamberti et al. [55] compared the performance of MWCNTs with SWCNTs. The propagation delay time was analyzed at three different technologies 15, 21, and 32 nm by means of interval analysis. It was observed that for global interconnect lengths, the time delay obtained for MWCNT interconnects is less than 1 ns for the most severe configuration, i.e., for 15 nm technology node at a length of 250 µm, whereas for SWCNTs the delay is as large as 7.87 ns.

The estimation of performance parameters under the crosstalk influence is an important design concern in modern VLSI interconnects. The crosstalk analysis of MWCNTs has been studied by several researchers. Liang et al. [56] analyzed the crosstalk noise effects with lengths ranging from 10 to 1000 µm at 22 and 14 nm

technology nodes. Moreover, the performance of MWCNTs was compared with the Cu interconnects. They observed that the MWCNT interconnects showed better performance for longer wire lengths and smaller technology nodes. Das et al. [57] analyzed the crosstalk effects in Cu, SWCNT, and MWCNT interconnects. They observed that the MWCNT-based interconnects are more suitable for VLSI interconnects. Furthermore, the authors analyzed the power supply voltage drop for Cu- and MWCNT-based interconnects in [58]. It was observed that the CNT-based interconnects have significantly less power drop in comparison to that of Cu-based interconnects for semi-global and global lengths. Based on the ESC model, Liang et al. [59] investigated the crosstalk effects in Cu and MWCNT interconnects. They reported that the crosstalk-induced time delays in MWCNT interconnects are much smaller than those in the Cu interconnects. Sahoo and Rahaman [60] developed an analytical closed-form delay expression for both Cu and MWCNT interconnects. They observed that the performance of MWCNT interconnects over copper interconnects is improved by 90 % for 200 μm long interconnect. In 2015, Tang et al. [61] proposed a fast transient simulation technique based on the ESC model for the crosstalk-induced performance analysis of MWCNT interconnects. They observed that the proposed method and HSPICE are very similar to each other with an average relative error of 1.54 %. However, most of the researchers [56, 59–61] used the resistive driver in the performance analysis of MWCNT interconnects that leads to severe errors in the performance estimation of the driver-interconnect-load (DIL) systems.

2.3 Graphene Nanoribbons

In 1996, Mitsutaka Fujita and his group provided a theoretical model of graphene nanoribbons (GNRs) to observe the edge and nanoscale dimension effect in graphene [62, 63]. Recent developments in GNRs have aroused a lot of research interest of their potential applications in the area of interconnects and field-effect transistors [64–66]. A monolithic system can be constructed using the single-layer GNR for both transistors and interconnects. For nanoscale device dimensions, Cu-based interconnects are mostly affected by grain boundaries and sidewall scatterings. It has been predicted that GNRs will outperform the Cu interconnects for smaller widths [67]. In a high-quality GNR sheet, the mean free path is ranging from 1 to 5 μm. GNRs can carry large current densities of more than 10^8 A/cm^2. They also offer high carrier mobility that can reach up to 10^5 cm^2/(Vs) [68].

2.3.1 Basic Structure of GNRs

A graphene nanoribbon is a single sheet of graphene layer, which is extremely thin and limited in width, such that it results in a one-dimensional structure [69]. As a

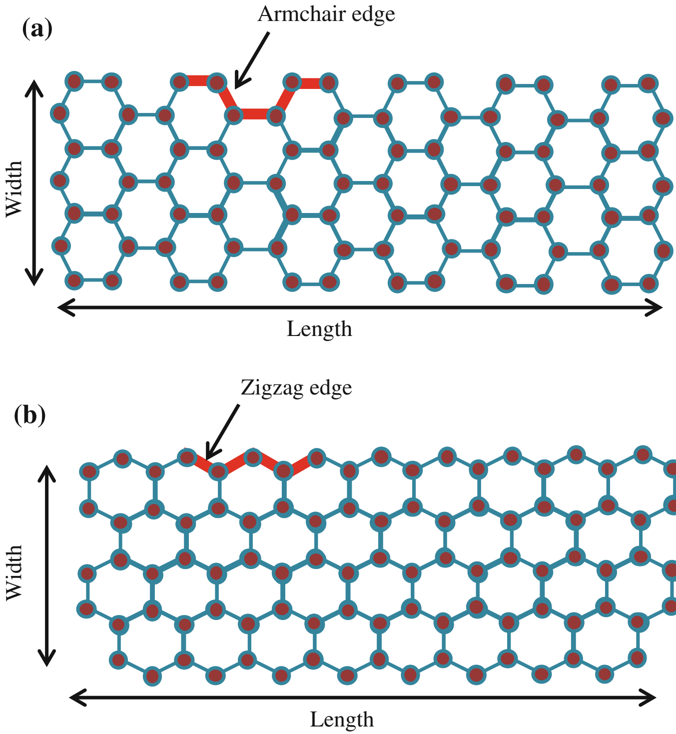

Fig. 2.13 Structure of GNR **a** armchair and **b** zigzag

result, GNRs can be considered as an unrolled version of CNTs. The electronic properties of GNRs are similar to that of CNTs. Depending on termination of their width, GNRs can be divided into chiral and nonchiral GNRs. The chiral GNRs can be further classified as armchair (ac) or zigzag (zz) GNRs as shown in Fig. 2.13a, b, respectively. It can be noted that the terms "armchair" and "zigzag" are used for both GNRs and CNTs. However, these nomenclatures are used in opposite ways. For GNRs the terms armchair and zigzag indicate the pattern of the GNR edge, whereas for CNTs the same terms indicate the CNT circumference. Therefore, the unrolled armchair CNT can be visualized as a zigzag GNR and vice versa.

Depending on the stacked graphene sheets, GNRs are classified as single-layer GNR (SLGNR) or multilayer GNR (MLGNR). The most promising interconnect solution for VLSI interconnect is MLGNR due to its higher current carrying capability than SLGNR. The geometric structure of an MLGNR is shown in Fig. 2.14. The MLGNR interconnect consists of N number of layers, with interlayer distance δ, width w, and thickness t.

From the fabrication point of view, it is evident that the growth of the GNRs can be more easily controlled than that of the CNTs because of their planar structure. This makes them compatible with the conventional lithography techniques [70].

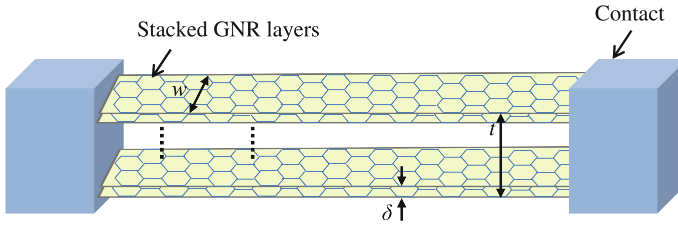

Fig. 2.14 The geometric structure of an MLGNR interconnect

Using the electron beam lithography technique, Murali et al. [71] fabricated an MLGNR interconnect with ten layers. The higher electrical conductivity in MLGNR can be obtained either by enhancing the carrier mobility or by increasing the number of carriers. The carrier mobility can be increased by intercalation doping of arsenic pentafluoride (AsF_5) vapor. Using the AsF_5 doping, the conductivity of MLGNR can be increased up to 3.2×10^5 S/cm, which is almost 1.5 times higher than the copper interconnects [72]. Additionally, the easier fabrication process of MLGNRs makes them as promising candidates for interconnect material.

2.3.2 *Semiconducting and Metallic GNRs*

GNRs can act as either semiconducting or metallic based on the pattern of the GNR edge. The zigzag edge-patterned GNR always act as metallic, whereas the armchair edge-patterned GNRs can act as either metallic or semiconducting depending on the number of carbon atoms present across the width of the GNR. This section presents the behavior of armchair GNRs and its dual nature.

The typical structure of armchair GNR is shown in Fig. 2.13a, where the number of carbon atoms across its width, $N_C = 7$. For understanding the metallic/semiconducting behavior of GNRs, it is necessary to analyze the electronic band structures. The band structures of GNRs are obtained using a tight-binding (TB) model [73]. Using the TB approach, the band structures of 23- and 24-atom wide armchair GNRs are shown in Fig. 2.15a, b, respectively. It can be observed that the metallic GNR has zero bandgap, whereas the semiconducting GNR has 0.2 eV bandgap. The ac GNR acts as metallic, if $N_C = 3a + 2$ and acts as semiconducting, if $N_C = 3a + 1$ or 3, where a is an integer. The zz GNRs are always metallic, independent of the value of N_C [73].

2.3.3 *Properties and Characteristics of GNRs*

Most of the physical and electrical properties of GNRs are similar to that of CNTs. However, compared to CNTs, the growth of the GNRs is considered to be more

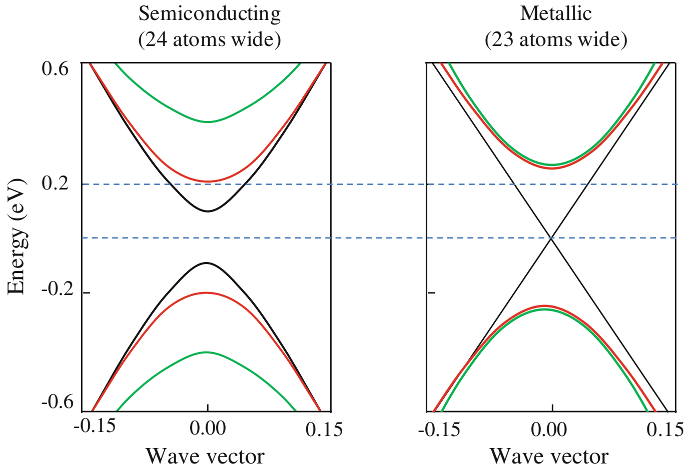

Fig. 2.15 Band structures of **a** semiconducting and **b** metallic armchair GNRs whose widths are 6.02 nm (24 atoms wide) and 5.78 nm (23 atoms wide), respectively

controllable due to their planar structure. Moreover, the major advantage of GNRs over CNTs is that both transistor and interconnect can be fabricated on the same continuous graphene layer, which unlike CNTs, are free from Stone–Wales defects [74]. Therefore, one of the manufacturing difficulties regarding the formation of metal–nanotube contact can be avoided. Due to the lower resistivity, the MLGNRs are often preferred over SLGNRs as suitable on-chip interconnect material. However, the MLGNRs fabricated till date, have displayed some level of edge roughness [70, 71]. The electron scattering at the rough edges reduces the mean free path that substantially lowers the conductance of the MLGNR. This fundamental challenge limits the performance of MLGNR-based interconnects. The value of MFP primarily depends on the level of edge roughness. The following sections discuss the effect of edge roughness on the MFP.

2.3.3.1 Mean Free Path of GNR

The effective MFP of GNR λ_{eff} depends on the scattering effects due to phonons λ_{ph}, defects λ_d, and edge roughness λ_n. Using Matthiessen's rule, the λ_{eff} can be expressed as

$$\frac{1}{\lambda_{\text{eff}}} = \frac{1}{\lambda_d} + \frac{1}{\lambda_n} + \frac{1}{\lambda_{\text{ph}}} \tag{2.18}$$

For the interconnect applications (low bias), the MFP corresponding to λ_{ph} is observed as extremely large, i.e., tens of micrometers, and therefore, its effect can

be neglected for the modeling of GNR scattering resistance [73]. Consequently, λ_d and λ_n dominate the overall value of λ_{eff}.

According to the experimental measurements reported in [75], the MFP corresponding to λ_d is about 1 μm for a single-layer GNR, which is width independent. However, in multilayer GNR, the MFP reduces due to the intersheet electron hopping [76]. The λ_d of MLGNR can be extracted by measuring the in-plane conductivity of GNR. Using the in-plane conductivity of $G_{\mathrm{sheet}} = 0.026\ (\mu\Omega\text{-cm})^{-1}$ [77], layer spacing of 0.34 nm, and $E_F = 0$ of a neutral MLGNR, the λ_d is extracted as 419 nm by solving Eq. (2.19) [77]

$$G_{\mathrm{sheet}} = \frac{2q^2}{h} \cdot \frac{\pi \lambda_d}{h v_f} \cdot 2k_B T \ln\left[2\cosh\left(\frac{E_F}{2k_B T}\right)\right] \tag{2.19}$$

To increase the conductivity of MLGNR, AsF_5 intercalated graphite can be used. The in-plane conductivity, $G_{\mathrm{sheet}} = 0.63\ (\mu\Omega\text{-cm})^{-1}$ and carrier concentration, $n_p = 4.6 \times 10^{20}\ \mathrm{cm}^{-3}$ are observed for the AsF_5 intercalated graphite [78]. Using the simplified TB model, the E_F can be expressed as

$$E_F = h v_F \left(\frac{n_p \cdot \delta}{4\pi}\right)^{1/2} \tag{2.20}$$

where $\delta = 0.575$ nm is the average layer spacing between adjacent graphene layers. Using the expressions (2.19) and (2.20), E_F and λ_d are expressed as 0.6 eV and 1.03 μm, respectively.

The MFP corresponds to diffusive scattering at the edges is a function of edge backscattering probability, P and the average distance by an electron travels along the length before hitting the edge. The mean free path for nth subband due to edge scattering can be expressed as [67]

$$\lambda_n = \frac{w}{P}\sqrt{\left(\frac{E_F/\Delta E}{n}\right)^2 - 1} \tag{2.21}$$

where ΔE is the gap between the subbands.

2.3.4 Conductivity Comparison

The performance of the interconnect line is primarily depends on the conductivity of the material. This section discusses the conductivity of various interconnect materials. Figure 2.16 shows the conductivity of Cu, SWCNT bundle, MWCNT and MLGNR interconnects. The fully specular edge MLGNR interconnects are analyzed for two different doped conditions [79]. First, the Fermi energy level of 0.3 eV is considered and second, the level of 0.6 eV is considered. The SWCNT

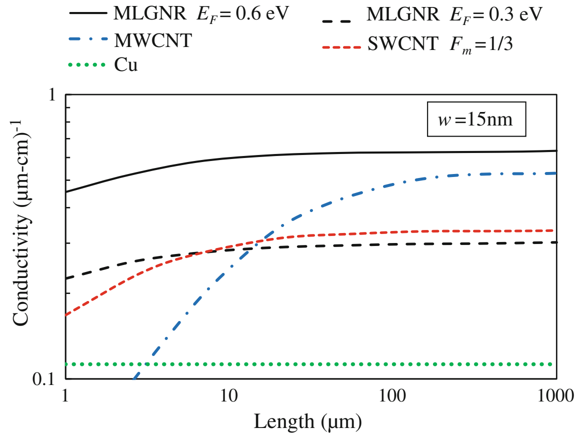

Fig. 2.16 Conductivity comparison among Cu, SWCNT bundle, MWCNT and MLGNR interconnects

diameter is chosen to be 1 nm with a metallic to semiconducting ratio (F_m) of 1/3. For MWCNTs, the outer diameter of CNT shell is considered as 15 nm. From Fig. 2.16, it can be observed that the conductivity of MLGNR increases with the Fermi energy. Moreover, at highly doped condition (E_F = 0.6 eV) the conductivity of MLGNR is observed to be higher than MWCNT interconnects.

2.3.5 MLGNR Interconnect Modeling

This section presents an electrical equivalent model of the MLGNR interconnect line. An MLGNR of width w and thickness t is placed above the ground plane at a distance H as shown in Fig. 2.17. The permittivity of the medium between the bottommost layer of MLGNR and the ground plane is represented by ε. The total number of layers (N_{layer}) can be expressed as

$$N_{\text{layer}} = 1 + \text{int}\left[\frac{t}{\delta}\right] \tag{2.22}$$

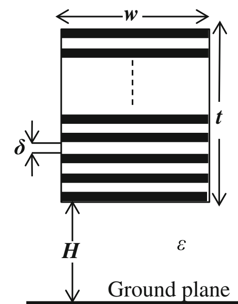

Fig. 2.17 Geometry of MLGNR above ground plane

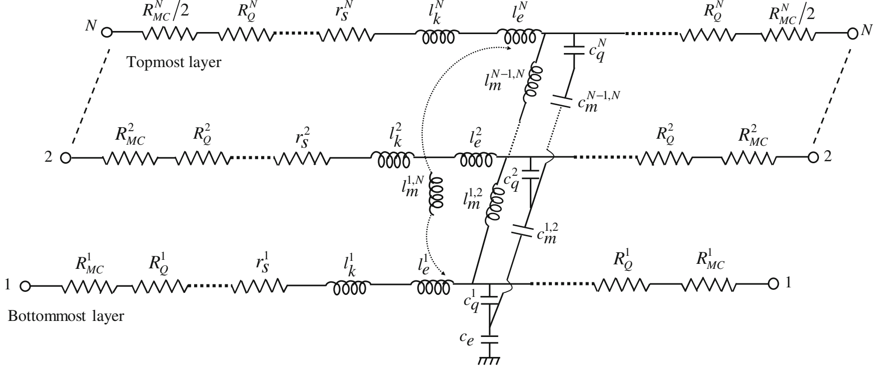

Fig. 2.18 Equivalent *RLC* model of MLGNR interconnect

The interlayer distance δ is considered to be 0.575 and 0.34 nm for doped and neutral MLGNRs [77], respectively.

The equivalent electrical model of MLGNR interconnect is presented in Fig. 2.18, wherein the parasitics are primarily dependent on the number of conducting channels (N_{ch}) of each layer in MLGNR. The N_{ch} takes into account the effect of spin and sublattice degeneracy of carbon atoms and primarily depends on the width, Fermi energy (E_F), temperature (T) and can be expressed as [80]

$$N_{\text{ch}} = \sum_{n=0}^{n_C} \left[e^{(E_i - E_F)/kT} + 1 \right]^{-1} + \sum_{n=0}^{n_V} \left[e^{(E_i + E_F)/kT} + 1 \right]^{-1} \tag{2.23}$$

where k, n_C, and n_V represent the Boltzmann constant, number of conduction and valence bands, respectively. E_i is the lowest/highest energy of ith subband in conduction/valence band [80].

Depending on the current fabrication process, the imperfect metal–MLGNR contact resistance (R_{MC}) has a typical value ranging from 1 to 20 kΩ [81]. Each layer of MLGNR exhibits lumped quantum resistance (R_Q) that is due to the quantum confinement of carriers across the interconnect width. The quantum resistance of jth layer (R_Q^j) can be expressed as

$$R_Q^j = \frac{h}{4e^2 \cdot N_{\text{ch}}} \tag{2.24}$$

For longer interconnects, scattering resistance r_s appears due to the static impurity scattering, defects, line edge roughness scattering (LER), etc. [82–84]. The r_s primarily depends on the effective MFP of electrons (λ_{eff}) and can be expressed as

$$r_s^j = \frac{h}{2e^2 \cdot N_{\text{ch}} \cdot \lambda_{\text{eff}}} \tag{2.25}$$

Using the Matthiessen's rule, the λ_{eff} of each subband can be expressed from (2.18). Each layer in MLGNR comprises of kinetic inductance (l_k) and quantum capacitance (c_q) that represent the mobile charge carrier inertia and the density of electronic states, respectively. The l_k and c_q of any layer j can be expressed as

$$l_k^j = \frac{l_{k0}}{2N_{\text{ch}}}; \text{where } l_{k0} = \frac{h}{2e^2 v_F} \tag{2.26}$$

$$c_q^j = 2c_{q0} \cdot N_{\text{ch}}; \text{where } c_{q0} = \frac{2e^2}{hv_F} \tag{2.27}$$

where $v_F \approx 8 \times 10^5$ m/s represents the Fermi velocity of carriers in graphene [81]. The kinetic inductance per channel is 8 nH/μm, which is verified by the experimental observations also [85]. The electrostatic capacitance (c_e) is due to the electric field coupling between the bottom most layer of MLGNR and the ground plane. Therefore, the c_e is primarily dependent on the MLGNR width (w) and the distance (H) from the ground plane. Apart from this, the magnetic inductance (l_e) of MLGNR interconnect is due to the stored energies of carriers in the magnetic field. The l_e and c_e can be expressed as

$$l_e^j = \frac{\mu_0 \mu_r H}{w} \quad \text{and} \quad c_e = \frac{\varepsilon_0 \varepsilon_r w}{H} \tag{2.28}$$

The interlayer mutual inductance (l_m) and coupling capacitance (c_m) are mainly due to the magnetic and electric field coupling between the adjacent layers. The l_m and c_m can be expressed as

$$l_m^{j-1,j} = \frac{\mu_0 \delta}{w}, \quad j = 2, 3, \ldots, N \tag{2.29a}$$

$$c_m^{j-1,j} = \frac{\varepsilon_0 w}{\delta}, \quad j = 2, 3, \ldots, N \tag{2.29b}$$

The analysis of signal propagation along an MLGNR with N_{layer} leads to the solution of a $2N$-dimensional system of differential equations that can be highly time-consuming. For this reason, the equivalent *RLC* model of Fig. 2.18 is simplified to an ESC model shown in Fig. 2.19, wherein all the layers are assumed to be parallel. The value of $R_1 = (R_{MC} + R_Q)$ is equally divided between the two contacts on either side of the interconnect line. The detailed explanation of ESC model of MLGNR interconnect line is provided in Sect. 5.2.

2.3.6 MLGNR Performance Analysis

The performance of an MLGNR interconnect is generally evaluated by means of an electrical equivalent model. The equivalent model considers all the parasitic

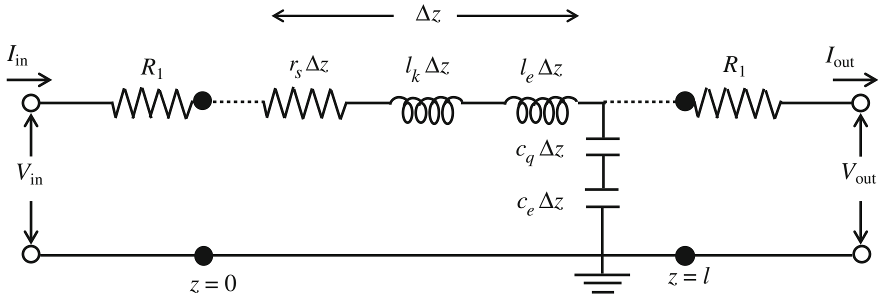

Fig. 2.19 Equivalent single conductor (ESC) model of MLGNR interconnect

parameters based on the quantum effects of the nanowire, and its electrostatic and magnetostatic characteristics. Sarto et al. proposed an electrical equivalent transmission model to represent the MLGNR interconnect [86]. They compared the performance between MWCNT and MLGNR interconnects and observed that the MLGNR interconnect has higher current carrying capability than the MWCNT interconnect. Xu et al. [77] derived the conductance model of MLGNR interconnect using the tight-binding approach and the Landauer formula. The conductance of the MLGNR is compared among Cu, W, and CNTs. They observed that the conductance of MLGNR is much higher than Cu, W, and CNTs when proper intercalation-doped MLGNRs are used. Nishad et al. [87] presented the analytical time domain models for the performance analysis of top contact and side contact MLGNR interconnects. Based on the analytical models, they designed an optimum top-contacted MLGNR interconnect that exceeds the performance of Cu and optical interconnects.

The crosstalk-induced signal transmission analysis of MLGNR interconnects was performed by Cui et al. [81] based on the transmission line model. The authors obtained the output response of driver-interconnect-load system using the transfer function. The impact of Fermi level on the signal transmission was also investigated. In 2014, Zhao et al. [79] performed the comparative study on MLGNR interconnects with SWCNT, MWCNT, and Cu interconnects. They observed that even with the maximum crosstalk impacts considered, the advantage of MLGNR interconnects over other interconnect materials can still be maintained. The impact of MLGNR line resistance variations on the crosstalk-induced performance parameters were investigated in [88]. The simulations were performed for 11 and 8 nm technology nodes for both intermediate and global interconnect lengths. They observed that irrespective of technology node, the perfectly doped fully specular MLGNR interconnects are better than Cu interconnects as far as the line resistance tolerance was concerned. However, the existing crosstalk noise models [79, 81, 88] analyzed the performance of MLGNR interconnects with resistive drivers that limits the accuracy of the models. Moreover, the authors considered the mean free path parameter independent of width by assuming perfectly smooth edges of MLGNRs.

References

1. Livshits P, Sofer S (2012) Aggravated electromigration of copper interconnection lines in ULSI devices due to crosstalk noise. IEEE Trans Device Mater Reliab 12(2):341–346
2. Moll F, Roca M, Rubio A (1998) Inductance in VLSI interconnection modeling. IEEE Proc Circuits Devices Syst 145(3):175–179
3. Sakurai T, Newton R (1990) Alpha-power law MOSFET model and its applications to CMOS inverter delay and other formulas. IEEE J Solid-State Circuits 25(2):584–594
4. Bowman KA, Austin BL, Eble JC, Xingha T, Meindl JD (1999) A physical alpha-power law MOSFET model. IEEE J Solid State Circuits 34(10):1410–1414
5. Dutta S, Shetti SSM, Lusky SL (1995) A comprehensive delay model for CMOS inverters. IEEE J Solid-State Circuits 30(8):864–871
6. Bisdounis L, Nikolaidis S, Koufopavlou O (1998) Analytical transient response and propagation delay evaluation of the CMOS inverter for short-channel devices. IEEE J Solid-State Circuits 33(2):302–306
7. Qian J, Pullela S, Pillage L (1994) Modeling the effective capacitance for the RC interconnect of CMOS gates. IEEE Trans Comput Aided Des 13(12):1526–1535
8. Hafed M, Oulmane M, Rumin NC (2001) Delay and current estimation in a CMOS inverter with an RC load. IEEE Trans Comput Aided Des 20(1):80–89
9. Chatzigeorgiou A, Nikolaidis S, Tsoukalas I (2001) Modeling CMOS gates driving RC interconnect loads. IEEE Trans Circuits Syst II Analog Digital Signal Process 48(4):413–418
10. Adler V, Friedman EG (1998) Repeater design to reduce delay and power in resistive interconnect. IEEE Tran Circuits Syst II Analog Digital Signal Process 45(5):607–616
11. Bakoglu HB, Meindl JD (1985) Optimal interconnection circuits for VLSI. IEEE Trans Electron Devices 32(5):903–909
12. Rubinstein J, Penfield P, Horowitz MA (1983) Signal delay in RC tree networks. IEEE Trans Comput Aided Des 2(3):202–211
13. Kahng A, Muddu S (1997) An analytical delay model for RLC interconnects. IEEE Trans Comput Aided Des 16(2):1507–1514
14. Ismail YI, Friedman EG, Neves JL (2000) Equivalent elmore delay for RLC trees. IEEE Trans Comput Aided Des 19(1):83–97
15. Bai X, Chandra R, Dey S, Srinivas PV (2004) Interconnect couplingaware driver modeling in static noise analysis for nanometer circuits. IEEE Trans Comput Aided Des 23(8):1256–1263
16. Davis JA, Meindl JD (2000) Compact distributed RLC models, part I: single line transient, time delay, and overshoot expressions. IEEE Trans Electron Devices 47(11):2068–2077
17. Davis JA, Meindl JD (2000) Compact distributed RLC models, part II: coupled line transient expressions and peak crosstalk in multilevel networks. IEEE Trans Electron Devices 47(11):2078–2087
18. Agarwal K, Sylvester D, Blaauw D (2006) Modeling and analysis of crosstalk noise in coupled RLC interconnects. IEEE Trans Comput Aided Des Integr Circuits Syst 25(5):892–901
19. Liu T, Kuo J, Zhang S (2012) A closed-form analytical transient response model for on-chip distortion less interconnect. IEEE Trans Electron Devices 59(12):3186–3192
20. Kaushik BK, Sarkar S (2008) Crosstalk analysis for a CMOS gate driven inductively and capacitively coupled interconnects. Microelectron J 39(12):1834–1842
21. Kaushik BK, Sarkar S, Agarwal RP, Joshi RC (2010) An analytical approach to dynamic crosstalk in coupled interconnects. Microelectron J 41(2):85–92
22. Li XC, Ma JF, Swaminathan M (2011) Transient analysis of CMOS gate driven RLGC interconnects based on FDTD. IEEE Trans Comput Aided Des Integr Circuits Syst 30(4): 574–583
23. Kroto HW, Heath JR, O'Brien SC, Curl RF, Smalley RE (1985) C_{60}: buckminsterfullerene. Nature 318:162–163
24. Scarselli M, Castrucci P, Crescenzi M (2012) Electronic and optoelectronic nano-devices based on carbon nanotubes. J Phys Condens Matter 24(31):313202-1–313202-36

25. Xu T, Wang Z, Miao J, Chen X, Tan CM (2007) Aligned carbon nanotubes for through-wafer interconnects. Appl Phys Letts 91(4):042108-1–042108-3
26. Monthioux M, Serp P, Flahaut E (2010) Introduction to carbon nanotubes. In: Bhushan B (ed) Handbook of nano-technology. Springer, New York
27. Wang N, Tang ZK, Li GD, Chen JS (2000) Single-walled 4 Å carbon nanotube arrays. Nature 408:50–51
28. Javey A, Kong J (2009) Carbon nanotube electronics. Springer
29. Hamada N, Sawada SI, Oshiyama A (1992) New one-dimensional conductors, graphite microtubules. Phys Rev Lett 68:1579–1581
30. Li HJ, Lu WG, Li JJ, Bai XD, Gu CZ (2005) Multichannel ballistic transport in multiwall carbon nanotubes. Phys Rev Lett 95(8):86601
31. Nihei M, Kondo D, Kawabata A (2005) Low-resistance multi-walled carbon nanotube vias with parallel channel conduction of inner shells. In: Proceedings of the IEEE international interconnect technology conference, pp 234–36
32. Forró L, Schönenberger C (2000) Physical properties of multi-wall nanotubes in topics in applied physics, carbon nanotubes: synthesis, structure, properties and applications. In: Dresselhaus MS, Dresselhaus G, Avouris P (eds) Springer-Verlag, Berlin, Germany
33. Wei BQ, Vajtai R, Ajayan PM (2001) Reliability and current carrying capacity of carbon nanotubes. Appl Phys Lett 79(8):1172–1174
34. Close GF, Wong HSP (2008) Assembly and electrical characterization of multiwall carbon nanotube interconnects. IEEE Trans Nanotechnol 7(5):596–600
35. Shah TK, Pietras BW, Adcock DJ, Malecki HC, Alberding MR (2013) Composites comprising carbon nanotubes on fiber. US Patent, US8585934 B2
36. Dresselhaus M, Dresselhaus G, Avouris Ph (2001) Carbon nanotubes: synthesis, structure, properties and applications. Top Appl Res 80
37. Hsieh JYL, Huang JM, Hwang CC (2006) Theoretical variations in the young's modulus of single-walled carbon nanotubes with tube radius and temperature: a molecular dynamics study. Nanotechnology 17:3920–3924
38. Forro L, Salvetat JP, Bonard J (2002) Electronic and mechanical properties of carbon nanotubes. In: Tománek D, Enbody RJ (eds) Science and application of nanotubes. Plenum Publishers, New York, pp 297–320
39. Wei C, Srivastava D, Cho K (2002) Thermal expansion and diffusion coefficients of carbon nanotube-polymer composites. Nano Lett 2(6):647–650
40. Wang Z, Zhao GL (2013) Microwave absorption properties of carbon nanotubes-epoxy composites in a frequency range of 2-20 GHz. Open J Compos Mater 3(2):17–23
41. Ifeanyi HN, John IE, Zhou W, Diola B, Guang-Lin Z (2015) Microwave absorption properties of multi-walled carbon nanotube (outer diameter 20–30 nm)–epoxy composites from 1 to 26.5 GHz. Diam Relat Mater 52:66–71
42. Srivastava A, Xu Y, Sharma AK (2010) Carbon nanotubes for next generation very large scale integration interconnects. J Nanophotonics 4(1):1–26
43. Li H, Yin WY, Banerjee K, Mao JF (2008) Circuit modeling and performance analysis of multi-walled carbon nanotube interconnects. IEEE Trans Electron Devices 55(6):1328–1337
44. Naeemi A, Meindl JD (2006) Compact physical models for multiwall carbon-nanotube interconnects. IEEE Electron Device Lett 27(5):338–340
45. Naeemi A, Sarvari R, Meindl JD (2005) Performance comparison between carbon nanotube and copper interconnects for gigascale integration (GSI). IEEE Electron Device Lett 26(2): 84–86
46. Burke PJ (2002) Lüttinger liquid theory as a model of the gigahertz electrical properties of carbon nanotubes. IEEE Trans Nanotechnol 1(3):129–144
47. Avouris P, Appenzeller J, Martel R, Wind SJ (2003) Carbon nanotube electronics. Proc IEEE 91(11):1772–1784
48. Li J, Ye Q, Cassell A, Ng HT, Stevens R, Han J, Meyyappan M (2003) Bottom-up approach for carbon nanotube interconnects. Appl Phys Lett 82(15):2491–2493

49. Ngo Q, Petranovic D, Krishnan S, Cassell AM, Ye Q, Li J, Meyyappan M, Yang CY (2004) Electron transport through metal–multiwall carbon nanotube interfaces. IEEE Trans Nanotechnol 3(2):311–317
50. Miano G, Villone F (2005) An integral formulation for the electrodynamics of metallic carbon nanotubes based on a fluid model. IEEE Trans Antennas Propag 54(10):2713–2724
51. Xu Y, Srivastava A (2009) A model for carbon nanotube interconnects. Int J Circuit Theory Appl 38(6):559–575
52. Sarto MS, Tamburrano A (2010) Single conductor transmission-line model of multiwall carbon nanotubes. IEEE Trans Nanotechnol 9(1):82–92
53. Tang M, Lu J, Mao J (2012) Study on equivalent single conductor model of multi-walled carbon nanotube interconnects. In: Proceedings of the IEEE Asia Pacific microwave conference, Taiwan, pp 1247–1249
54. D'Amore M, Sarto MS, Tamburrano A (2010) Fast transient analysis of next-generation interconnects based on carbon nanotubes. IEEE Trans Electromagn Compat 52(2):496–503
55. Lamberti P, Tucci V (2012) Impact of variability of the process parameters on CNT-based nanointerconnects performances: a comparison between SWCNTs bundles and MWCNT. IEEE Trans Nanotechnol 11(5):924–933
56. Liang F, Lin H, Wang G (2010) Prediction of crosstalk effects in future multiwall carbon nanotube (MWCNT) interconnects. In: Proceedings of the IEEE symposium on antennas propagation and EM theory (ISAPE), Guangzhou, pp 1031–1034
57. Das D, Rahaman H (2011) Analysis of crosstalk in single- and multiwall carbon nanotube interconnects and its impact on gate oxide reliability. IEEE Trans Nanotechnol 10(6): 1362–1370
58. Das D, Rahaman H (2011) IR drop analysis in single- and multi-wall carbon nanotube power interconnects in sub-nanometer designs. In: Proceedings of the IEEE Asia symposium on quality electronic design (ASQED), pp 174–183
59. Liang F, Wang G, Lin H (2012) Modeling of crosstalk effects in multiwall carbon nanotube interconnects. IEEE Trans Electromagn Compat 54(1):133–139
60. Sahoo M, Rahaman H (2013) Performance analysis of multiwalled carbon nanotube bundles. In: Electronics and Nanotechnology (ELNANO), IEEE XXXIII international scientific conference, pp 200–204
61. Tang M, Mao J (2015) Modeling and fast simulation of multiwalled carbon nanotube interconnects. IEEE Trans Electromagn Compat 57(2):232–240
62. Fujita M, Wakabayashi K, Nakada K, Kusakabe K (1996) Peculiar localized state at zigzag graphite edge. J Phys Soc Jpn 65(7):1920–1923
63. Nakada K, Fujita M, Dresselhaus G, Dresselhaus MS (1996) Edge state in graphene ribbons: nanometer size effect and edge shape dependence. Phys Rev 54(24):17954–17961
64. Echtermeyer TJ, Lemme MC, Baus M, Szafranek BN, Geim AK, Kurz H (2008) Nonvolatile switching in graphene field-effect devices. IEEE Electron Device Lett 29(8):952–954
65. Lemme MC, Echtermeyer TJ, Baus M, Kurz H (2007) A graphene field-effect device. IEEE Electron Device Lett 28(4):282–284
66. Rawat B, Paily R (2015) Analysis of graphene tunnel field-effect transistors for analog/RF applications. IEEE Trans Electron Devices 62(8):2663–2669
67. Naeemi A, Meindl JD (2007) Conductance modeling for graphene nanoribbon (GNR) interconnects. IEEE Electron Device Lett 28(5):428–431
68. Li H, Xu C, Srivastava N, Banerjee K (2009) Carbon nanomaterials for next-generation interconnects and passives: physics, status and prospects. IEEE Trans Electron Devices 56(9):1799–1821
69. Kan, E.; Li, Z.; Yang. J. "Graphene nanoribbons: geometric electronic and magnetic properties," In *Physics and Applications of Graphene—Theory*, *INTECH,* ed. S. Mikhailov, Chapter 16, 2011.
70. Avouris P (2010) Graphene: electronic and photonic properties and devices. Nano Lett 10(11):4285–4294

71. Murali KH, Brenner K, Yang Y, Beck T, Meindl JD (2009) Resistivity of graphene nanoribbon interconnects. IEEE Electron Device Lett 30(6):611–613
72. Dresselhaus MS, Dresselhaus G (2002) Intercalation compounds of graphite. Adv Phys 51 (1):1–186
73. Naeemi A, Meindl JD (2009) Compact physics-based circuit models for graphene nanoribbon interconnects. IEEE Trans Electron Devices 56(9):1822–1833
74. Stan MR, Unluer D, Ghosh A, Tseng F (2009) Graphene devices, interconnect and circuits—challenges and opportunities. In: Proceedings of the IEEE international symposium on circuits and systems (ISCAS), Taipei, pp 69–72
75. Berger C, Song Z, Li X, Wu X, Brown N, Naud C, Mayou D, Li T, Hass J, Marchenkov AN, Conrad EH, First PN, Heer WA (2006) Electronic confinement and coherence in patterned epitaxial graphene. Science 312(5777):1191–1196
76. Benedict LX, Crespi VH, Louie SG, Cohen ML (1995) Static conductivity and superconductivity of carbon nanotubes—Relations between tubes and sheets. Phys Rev B Condens Matter 52(20):14935–14940
77. Xu C, Li H, Banerjee K (2009) Modeling, analysis, and design of graphene nanoribbon interconnects. IEEE Trans Electron Devices 56(8):1567–1578
78. Hanlon LR, Falardeau ER, Fischer JE (1977) Metallic reflectance of AsF_5-graphite intercalation compounds. Solid State Commun 24(5):377–381
79. Wen-Sheng Zhao; Wen-Yan Yin (2014) Comparative study on multilayer graphene nanoribbon (MLGNR) interconnects. IEEE Trans Electromagn Compat 56(3):638–645
80. Nasiri SH, Faez R, Moravvej-Farshi MK (2012) Compact formulae for number of conduction channels in various types of grapheme nanoribbons at various temperatures. Mod Phys Lett B 26(1):1150004-1–115004-5
81. Cui J, Zhao W, Yin W, Hu J (2012) Signal transmission analysis of multilayer graphene nano-ribbon (MLGNR) interconnects. IEEE Trans Electromagn Compat 54(1):126–132
82. Areshkin DA, Gunlycke D, White CT (2007) Ballistic transport in graphene nanostrips in the presence of disorder: importance of edge effects. Nano Lett 7(1):204–210
83. Hwang EH, Adam S, Sarma SD (2007) Carrier transport in two-dimensional graphene layers. Phys Rev Lett 98(18):186806-1–186806-4
84. Yan J, Zhang Y, Kim P, Pinczuk A (2007) Electric field effect tuning of electron-phonon coupling in graphene. Phys Rev Lett 98(16):166802-1–166802-4
85. Plombon JJ (2007) High-frequency electrical properties of individual and bundled carbon nanotubes. Appl Phys Lett 90(6):063106-1–063106-3
86. Sarto MS, Tamburrano A (2010) Comparative analysis of TL models for multilayer graphene nanoribbon and multiwall carbon nanotube interconnects. In: Proceedings of the IEEE international symposium on electromagnetic compatibility, Fort Lauderdale, FL, USA, pp 212–217
87. Nishad AK, Sharma R (2014) Analytical time-domain models for performance optimization of multilayer GNR interconnects. IEEE J Sel Top Quantum Electron 20(1):3700108-1–3700108-8
88. Sahoo M, Rahaman H (2014) Impact of line resistance variations on crosstalk delay and noise in multilayer graphene nano ribbon interconnects. In: Proceedings of the international symposium on electronic system Design (ISED), pp 94–98

http://www.springer.com/978-981-10-0799-6

Crosstalk in Modern On-Chip Interconnects
A FDTD Approach
Kaushik, B.K.; Kumar, V.R.; Patnaik, A.
2016, XV, 116 p. 71 illus., Softcover
ISBN: 978-981-10-0799-6